

Decoupling Local Electrostatic Potential and Temperature-Driven Atomistic Forming Mechanisms in $\text{TaO}_x/\text{HfO}_2$ -Based ReRAMs using Reactive Molecular Dynamics Simulations

Simanta Lahkar,[†] Valeria Bragaglia,^{‡,†} Behnaz Bagheri,[¶] Donato Francesco Falcone,[‡] Matteo Galetta,[‡] Marilyne Sousa,[‡] and Aida Todri-Sanial^{*,†}

[†]*NanoComputing Research Lab, Integrated Circuits Group, Electrical Engineering Department, Eindhoven University of Technology, Eindhoven, 5612AZ, The Netherlands*

[‡]*IBM Research Europe-Zurich, Rueschlikon, Switzerland*

[¶]*Department of Applied Physics, Eindhoven University of Technology, Eindhoven, 5612AZ, The Netherlands*

E-mail: a.todri.sanial@tue.nl

Abstract

Resistive random access memories (ReRAMs) with a bilayer $\text{TaO}_x/\text{HfO}_2$ stack structure have been shown to possess uniquely promising resistive switching characteristics. However, the key atomistic forming mechanisms and the physical processes that govern the behavior of this kind of device remain to be clarified. Here, we present a detailed analysis of the physical mechanisms underlying its forming at the atomistic level through molecular dynamics (MD) simulations using an extended charge equilibration scheme to describe the effects of applied voltage with the charge transfer ionic potential formalism. The displacement of the tantalum ions was found to be the highest,

followed by that of the hafnium ions, in response to a sufficiently high applied voltage across the electrodes, whereas the oxygen ions had a relatively minor voltage-driven response. This led to the formation of a tantalum-depleted, oxygen-rich zone near the positive top electrode acting as the anode and the clustering of oxygen vacancies that nucleated into the filament near the negative bottom electrode, or the cathode. This process resulted in partial shielding of the bulk dielectric from the applied voltage. We found a minimum threshold voltage was required to initiate vacancy clustering to form the filament. Filament growth during forming is attributed to a localized mechanism, driven by thermally activated generation of oxygen vacancy defects, which get stabilized by the local electric fields near the edge of the nucleated filament at the cathode.

Introduction

Resistive random access memories (ReRAMs), also known as memristors, are resistive switching devices that have gained significant attention for their potential in neuromorphic computing and non-volatile memory technologies.^{1,2} These devices are typically built using a metal-insulator-metal stack design, where the resistance of the insulator can be dynamically altered based on the history of charge flow through it.¹⁻⁴ However, typically, an initial process known as electroforming is required before this dynamic resistance change can occur. During electroforming, a high voltage is applied across the electrodes inducing the formation of a conductive filament within the insulating layer. Transition metal oxides (TMOs) such as TaO_x and HfO_2 are commonly used as the dielectric materials for this insulating layer in conventional ReRAMs due to their ability to generate and control oxygen vacancies that can cluster into a network of connected regions containing the oxygen-deficient phases of high conductivity within the dielectric, forming the filament.⁵⁻⁹ The structural evolution of and around this filament allows the device to switch between low- and high-resistance states, enabling the resistive switching behavior that ReRAMs are known for.^{1-4,10}

In recent years, bilayer ReRAM structures combining a layer of a conductive metal oxide (CMO) material, like TiO_x , TaO_x , and AlO_x , and a dielectric HfO_2 layer stacked together between inert electrodes have shown significant improvements over single-layer devices.^{11–14} These bilayer configurations offer enhanced analog bipolar switching, the ability to achieve multiple resistive states, and reduced noise and stochasticity in switching. Such properties make bilayer ReRAMs particularly attractive for energy-efficient neuromorphic computing applications, such as ReRAM-based crossbar arrays for accelerating deep neural network inference and training,^{15–18} as well as oscillatory neural networks (ONNs), where they act as tunable resistive coupling elements between oscillating neurons^{19,20} [also possible to cite recent IBM submission to IMW if available].

Experimental studies on $\text{TaO}_x/\text{HfO}_2$ -based ReRAMs have shown how CMO and HfO_x material properties impact their performance characteristics, like resistance range, switching behavior, and yield.^{14,15} Furthermore, a physics-based compact model accounting for the electrothermal response within these devices has been recently proposed that can simulate their switching behavior with high accuracy.^{21–23} However, despite the promising characteristics of bilayer ReRAMs, the literature lacks studies addressing their electroforming process from an atomistic perspective, which is crucial to clarify and validate the physical mechanisms underlying the behavior of these devices. On the other hand, the electroforming in conventional single-layer ReRAMs has been extensively studied, providing insights into their behavior and optimization of the device characteristics.^{5–10} However, the primary electroforming mechanism in TaO_x or HfO_2 -based ReRAMs remains a matter of contention in the literature, even for single-layer devices.^{8,10,24,25}

The behavior of single-layer TaO_x or HfO_2 -based ReRAMs has conventionally been attributed to the valence change mechanism (VCM).²⁶ In the VCM model, it is the electric field-driven migration of oxygen vacancies, which generate at the anode,^{27,28} that results in the formation of a conductive filament.^{3,9,26} This filament can break and reform, upon subsequent reversing of the voltage polarity applied to the electrode, enabling resistive switching.

Joule heating can further accelerate this process by providing the thermal energy necessary to enhance the electric field-driven migration of oxygen vacancies.³

In contrast, the behavior of some ReRAMs, such as those based on NiO, is explained by the thermochemical mechanism (TCM), where thermally activated conductivity increase in the metal oxide layer creates a hot channel, leading to ionic segregation driven by the thermal gradient in the radial direction around the channel and consequent filament formation.^{29–32} Recent experiments on single-layer TaO_x-based ReRAM with inert electrodes have revealed a two-stage forming process, characterized by thermal runaway followed by compositional runaway, which is indicative of the TCM.^{4,10} Other studies have also indicated that the thermal effects could be even more significant in the forming process of TaO_x and HfO₂-based ReRAMs than the electric field-driven effects, challenging the traditional distinction between VCM and TCM in these devices.^{8,24,25,33}

Additionally, some studies have suggested that the motion of tantalum atoms in TaO_x-based ReRAMs may be as prominent as that of the oxygen ions during filament formation.^{4,8,10} This is in apparent contrast with the expectation based on the diffusion constant of tantalum ions, which has been reported to be significantly lower than that of oxygen ions in the literature.³⁴ Thus, understanding the atomistic mechanisms within the TaO_x and HfO₂-based ReRAMs is crucial to reconcile these differences and to explain why they exhibit characteristics of both the VCM and TCM models. This becomes particularly important for clarifying the behavior of bilayer ReRAMs comprising both the TMO layers.

The focus of this study is to provide atomistic insights into the forming mechanisms of TaO_x/HfO₂-based bilayer ReRAM devices with inert electrodes, clarifying the roles of localized electric fields and thermal effects in this process. To achieve this, we perform all-atom reactive molecular dynamics (MD) simulations on a bilayer TaO_x/HfO₂ ReRAM stack model, using the charge transfer ionic potential (CTIP)^{35,36} combined with the electrochemical dynamics with implicit degrees of freedom (EChemDID) method for the application of an external voltage.³⁷ The CTIP is a kind of reactive force field proposed by Zhou *et al.*

that can model both the metallic and ionic interactions in a single formalism.³⁵ Coupled with the charge equilibration (QEq) scheme, it considers a radial distribution of electron densities instead of point charges and allows dynamic variation of atomic charges.^{38–40} CTIP is a modification of the original Streitz and Mintmire potential⁴¹ with added charge bounds, which overcomes several of its limitations and has been optimized to accurately model the redox reactions in a system comprising multiple metal oxides, including HfO_2 and TaO_x .^{40,42,43} Additionally, the EChemDID method has been shown to effectively model the propagation of applied voltage on the electrodes of an electrochemical cell through the conductive atoms in an all-atom MD simulation.^{9,44} We have implemented all the mentioned procedures in the Large-scale Atomic/Molecular Massively Parallel Simulator (LAMMPS) software to perform the reactive MD simulations under externally applied voltage in this study.⁴⁵

In this study, we created the atomistic model of the electrochemical cell that comprised of the $\text{TaO}_x/\text{HfO}_2$ stack sandwiched between inert electrodes based on scanning transmission electron microscopy (STEM) and Energy dispersive X-ray spectroscopy (EDX) characterization of the experimental bilayer ReRAM device. We applied a voltage of 1.2 V (referred to as 'High Voltage') across the device and derived key atomistic insights on the filament nucleation mechanisms, revealing the distinct interfacial effects and the physical origin of the varying ionic responses observed experimentally in TaO_x -based ReRAM devices. It is important to note that the maximum forming voltage in the bilayer ReRAM device could reach 5.85 V, after which its resistance begins to rapidly reduce as the temperature is expected to shoot up locally inside the device potentially undergoing a thermal and compositional runaway effect.^{10,14} However, the 1.2 V bias was found to be sufficiently high to distinctly observe not only the initialization of the filament formation within the device during our MD simulation but also to distinguish the differences in the structure of the formed filament when the device is heated to different temperatures, which is discussed in a later section of this paper. This allowed us to study the physical mechanisms at play during the electroforming process from an early stage before any temperature increase takes place and later

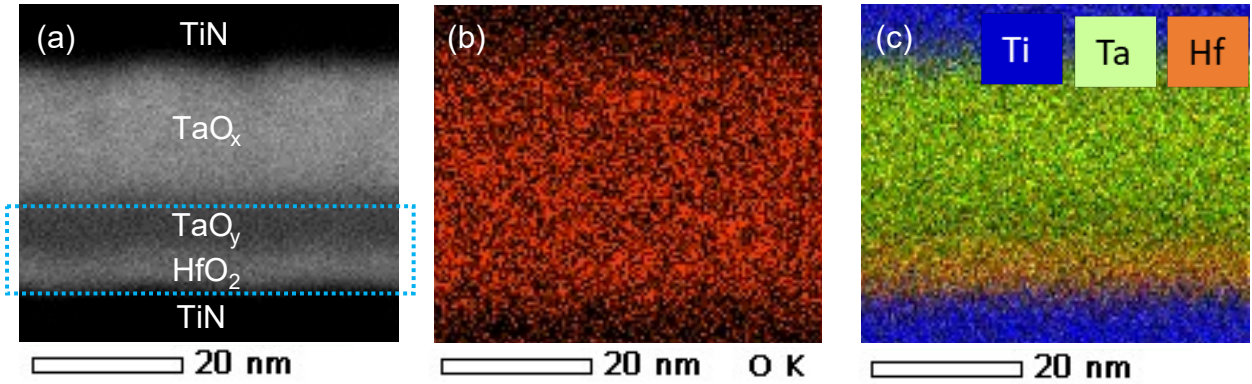


Figure 1: Cross-section images of the bilayer ReRAM. (a) STEM Bright Field image of the device cross-section. The dotted blue square highlights the two dielectric layers in the device that are oxygen-rich and amorphous. (b-c) EDX elemental maps of the device layer stack in (a).

distinguish the role of the temperature. We further observed the effect of Joule heating to accelerate filament growth, which aligned with experimental observations, not by enhancing the electric field-driven ion migration but by increasing the generation and aggregation of oxygen vacancies near the end of the seeded filament. Additionally, once we elucidate the mechanisms at play at the onset of forming in the device and the role of the thermal effects in this process, we focused on isolating the distinct role of the applied voltage on forming by simulating the device at a much lower voltage. The goal of this was to study the atomistic response in the device in a regime where the processes related to the forming have not yet begun and compare it with the results from our previous simulations under the high voltage conditions corresponding to the onset of forming in the device. Thus, we simulated the device response under a sufficiently 'Low Voltage' of 0.6 V, which allowed us to identify a threshold voltage that controlled forming by simply enabling the aggregation of vacancies into the filament.

Results and discussion

Device Layer Structure and Modeling Approach

We first obtain insights into the structure of an experimental TaO_x/HfO₂-based ReRAM device, which showed promising switching behavior,¹⁴ using transmission electron microscopy characterization to use as a reference for our atomistic model. Figure 1 shows the scanning transmission electron microscopy (STEM) cross-section of the device and the corresponding elemental distribution maps obtained using energy dispersive X-ray spectroscopy (EDX). These devices, fabricated by depositing an oxygen-deficient conductive TaO_x layer on top of the HfO₂ layer, develop another spurious interlayer between the two, as can be seen in Figure 1 (a). It can be seen from the EDX elemental maps that the same elements are present in both the upper TaO_x and the spurious layer of the device, hereafter referred to as the TaO_y layer in this paper. An EDX line scan, shown in Figure S1 of Supplementary Information (SI), indicates that the TaO_y could have a higher proportion of oxygen to tantalum than the TaO_x layer. Prior characterization on the same device has shown that the TaO_x layer is conductive while the oxygen-rich TaO_y and HfO₂ layers are amorphous and dielectric.^{14,46} Any electric field-assisted structural changes associated with the filament formation should initiate and occur within the regions with the highest resistivity in the device that also experience the highest potential drop during electroforming, as with the case for the region of interest governing the switching behavior.²³ Hence, we focused on the high-resistance TaO_y and HfO₂ layers, hereafter referred to as the *functional (bi)layers*, to simulate and understand the mechanisms governing the onset and progress of the electroforming process in these devices, and the conductive upper TaO_x layer was considered as an extension of the top electrode. Furthermore, the thickness of each of these two layers lies between 2 to 4 nm, while the total thickness of the device between TiN electrodes is about 25 nm.¹⁴ Additionally, both the TiN electrodes and the upper conductive TaO_x layer have low oxygen affinities, i.e., they do not have the tendency to accept or consume O ions from the dielectric matrix of the

device, and, hence, are not expected to exchange oxygen ions with the functional layers.^{14,47}

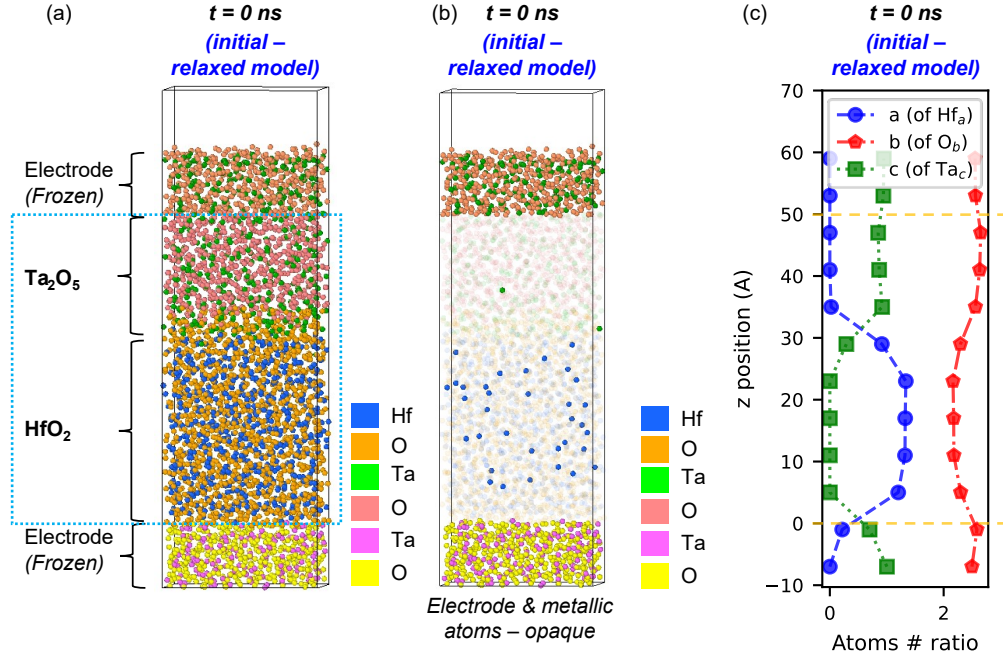


Figure 2: Structural characteristics of the relaxed $\text{Ta}_2\text{O}_5/\text{HfO}_2$ ReRAM atomistic model. (a) An atomic snapshot of the device stack model illustrating its different layers. The dotted blue square highlights the amorphous functional dielectric layers of the device, corresponding to the highlighted region of the STEM of the device cross-section Figure 1. (b) Distribution of conductive (undercoordinated metal) ions between the electrodes in the initial structure, illustrated by making the rest of the atoms semi-transparent. (c) Varying material composition, given by $\text{Hf}_a\text{Ta}_c\text{O}_b$, across the thickness of the relaxed device stack model. The a , b , and c values, corresponding to the proportion of Hf, O, and Ta atoms, respectively, in the structure at any position along the z -axis, are normalized so that $a + b + c$ equals 3.5. The upper and lower dotted yellow lines in the plot mark the location of the electrode/functional layer interfaces. The Tantalum and Oxygen atoms of the different layers are colored differently in the atomic snapshots for better visual distinction between the elements belonging to consecutive layers.

To model the functional layers of the device, we equilibrated a stack of oxygen-rich amorphous Ta_2O_5 layer on top of amorphous HfO_2 layer (Figure 2(a)), both of which were created independently through the melt-quench process,^{9,34} for 500 ps under 1 bar pressure and at 300 K temperature using the Nosé-Hoover thermostat and barostat.^{48,49} An upper 1 nm thick region of Ta_2O_5 top layer was defined as the top electrode, leaving behind a functional bilayer of 5 nm thickness. The interface of the top electrode with the rest of

the Ta_2O_5 layer corresponds to the interface of the upper conductive TaO_x layer with the TaO_y interlayer in the actual device (Figure 1 (a)).¹⁴ The material for the bottom electrode was also chosen as amorphous Ta_2O_5 with a thickness of 1 nm, similar to the top electrode, which allows the atomic interactions in the whole model to be defined consistently using the same interatomic potential optimized for metal oxide systems.⁴⁰ It was already clarified in a previous study that the observed characteristics of the $\text{TaO}_x/\text{HfO}_2$ -based ReRAM device cannot be attributed to any asymmetry between the work functions of the two electrodes.¹⁴ Furthermore, the atoms in both the electrodes were kept frozen during the MD simulations, modeling the low affinities of both the TiN electrode and TaO_x layer materials towards exchanging oxygen with the functional layers in the actual device. Since the MD simulations cover a much smaller timescale as compared to the actual electroforming process that takes several microseconds,¹⁰ keeping the electrodes frozen is a sufficiently valid approximation of the effect of low oxygen affinities of the electrodes to simulate the key atomistic processes within the device in that timescale.

The simulation cell for the device stack model (2 (a)) has a periodic boundary in x and y (lateral), and a fixed boundary in z (vertical) directions and with a 1 nm vacuum added above the top electrode. The final bilayer stack model of our device, as shown in Figure 2 (a), comprised a total functional layer thickness of 5 nm. To identify and define the conductive (metallic) ions in our device stack model, whose regional clustering could be used to track the evolution of the filament, an oxygen coordination ≤ 5 was adopted as the criterion for the metal atoms, following a previous study on HfO_2 -based electrochemical cell by Urquiza *et al.*⁹ The reasoning for this is based on previous first-principles studies that demonstrated conductive channels in metal/ HfO_2 /metal structures with filaments that comprised of 5-fold coordinated Hf atoms.⁵ We used the same maximum oxygen coordination criterion for both Ta and Hf atoms for simplicity and considering that the structure evolutions in the oxides of Ta and Hf with the change in O content are similar to each other.³⁴ The cluster analysis of these atoms was done using a cut-off of 3.9 Å to identify their largest non-simply connected

network, considered as the filament.⁹ We find that the conductive atoms are scattered more densely in the HfO₂ layer, with a more sparse distribution present in the Ta₂O₅ layer (2 (b)). This is because our adopted coordination criterion for conductive atoms is more strict with respect to the Ta₂O₅ layer than the HfO₂ owing to the higher oxygen percentage of the former. The profile of atomic distribution ratios in the relaxed structure shown in Figure 2 (c) reflects the bilayer Ta₂O₅ and HfO₂ stack design, with a small region of intermixing at the interface between the two functional layers.

Structural Changes on High Voltage Application across Electrodes

We first studied the structural changes occurring in the device at the onset of the electroforming process. To do this, we applied a voltage of 1.2 V across the electrodes with the top and the bottom electrodes acting as the positive (anode) and negative (cathode) electrodes, respectively, as shown in Figure 3 (a), and performed an MD simulation at 300 K for 500 ps in a canonical ensemble. We found that, on the application of this voltage, the scattered conductive ions in the initial structure depicted in Figure 2 (b) start to come closer together drifting downwards, and cluster at the cathode interface initializing the filament formation as shown in Figure 3 (a). Additionally, a notable increase in the ratio of oxygen-to-tantalum atoms was observed on top of the Ta₂O₅ functional layer at its interface with the anode (Figure 3 (b)). There was also an increase in the Hf percentage in the HfO₂ functional layer near its interface with the cathode, although it is not as significant a change as that near the anode (Figure 3 (b)) and can be attributed to the accumulation of the oxygen vacancies near the cathode associated with seeding of the filament. In order to understand the nature and origin of these structural changes during the early stages of the electroforming process, we took a deeper look at them from the ionic perspective.

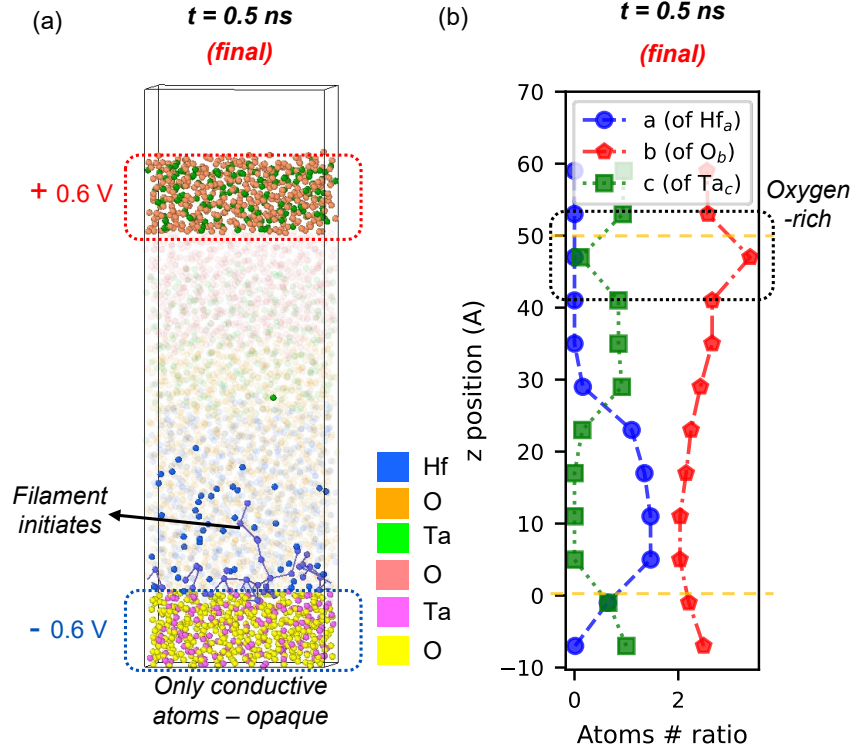


Figure 3: Structural characteristics of the bilayer stack model at the end of 500 ps of MD simulation at 300 K and with 1.2 V net voltage applied across the electrodes. (a) An atomic snapshot illustrating the initialization of filament formation by clustering of conductive metal atoms (analogous to sites of oxygen vacancies) in the functional layer near the cathode. Atoms in the functional layer that are not metallic are made semi-transparent for clarity. (b) The profiles of material composition, given by $\text{Hf}_a\text{Ta}_c\text{O}_b$, along the thickness of the final device stack structure. The a , b , and c values, corresponding to the proportion of Hf, O, and Ta atoms, respectively, in the structure at any position along the z -axis, are normalized so that $a + b + c$ equals 3.5. The upper and lower dotted yellow lines in the plot mark the location of the electrode/functional layer interfaces.

Ionic Response to High Voltage Application across Electrodes

We calculated the distribution of each ionic species across the thickness of our device stack model in the initial relaxed state and after the 500 ps room temperature simulation under the 1.2 V applied bias, as shown in Figure 4. We found no notable change in the distribution of oxygen atoms while a significant drop in the number of metal atoms, specifically of Ta ions, occurred near the anode (Figure 4(a-c)).

Hence, the development of the significant oxygen-rich region on top of the Ta_2O_5 func-

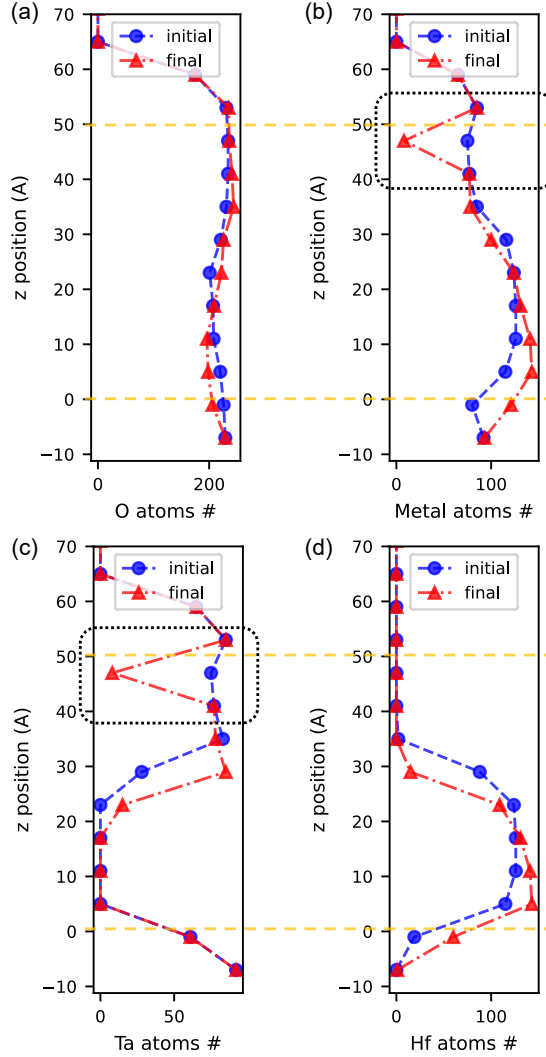


Figure 4: Change in distribution of different ionic species in the device stack over 500 ps MD simulation at 300 K under 1.2 V applied voltage. The distribution profiles of (a) oxygen, (b) metal, (c) Ta, and (d) Hf atoms in the initial (relaxed) and final device stack models across their thickness (z-direction). The dotted rectangles highlight the region near the anodic interface undergoing a drastic drop in the concentration of metallic Ta ions. The upper and lower dotted yellow lines in each subplot mark the location of the electrodes/functional layer interfaces.

tional layer at its interface with the anode, as noted from Figure 3 (b), could be attributed to a significant reduction in the Ta ion concentration, rather than an increase in the concentration of O ions near the anode, on the application of the voltage. Simultaneously, at the lower end of the HfO₂ functional layer, there occurred only a minor reduction in the O ion concentration while the population of Hf ions increased much more at the cathode interface,

as can be observed in Figure 4 (a and d).

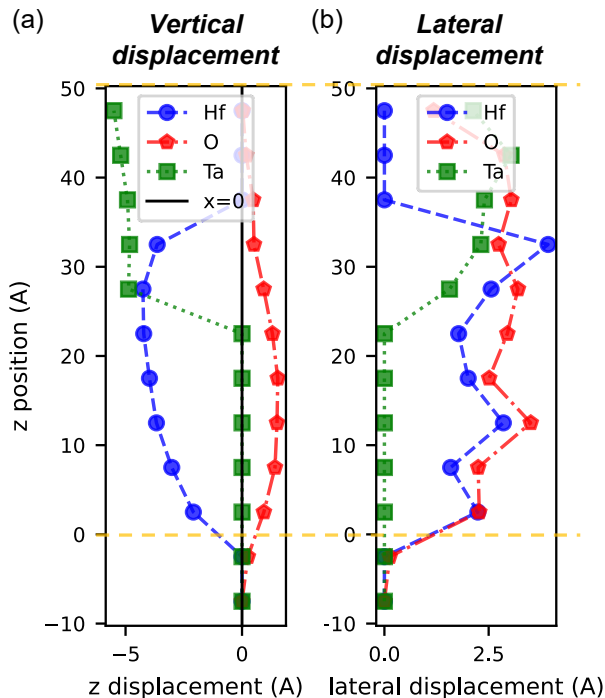


Figure 5: Variation in the motion of different ions across the device stack model under high voltage bias. The distribution profiles of net displacements of each atom type for varying initial positions along the thickness of the device stack model in (a) vertical and (b) lateral directions during 500 ps MD simulation at 300 K and under 1.2 V voltage difference applied across the electrodes. The upper and lower dotted yellow lines in each subplot mark the location of the interfaces of the functional layers with the anode and the cathode, respectively, in the device model.

Further insights into the ionic rearrangements within the device caused by the high voltage could be obtained by studying the directional displacements of each atomic species. Figure 5(a) shows the total voltage-driven displacements of each ionic species at different positions along the device thickness. The net displacements of the cations and anions were in the downward and upward directions, as expected from the polarity of the applied voltage (Figure 5(a)). We further observed that the downward displacements of the metallic ions were significantly higher than the upward displacement of the oxygen ions at any point across the device thickness (Figure 5(a)). In contrast, the net lateral motion, which is thermally activated, was similar for all the ionic species as revealed in Figure 5(b). Thus,

the reduction in metal ions (Figure 4 (b and c)), which created the oxygen-rich zone near the anodic interface of the Ta_2O_5 layer (Figure 3 (b)), was due to the Ta ions moving downwards away from the anode and into the functional layers of the device.

These results highlight a key difference in how the ionic species respond to the applied voltage: the Ta ions at the anode experience a much stronger repulsion than the oxygen ions at the cathode, leading to larger vertical displacements for the metal cations compared to the oxygen anions. To better understand these differences, we further analyzed the charge distribution on the various atomic species within the device stack model.

We first looked at the distribution of total charge across the thickness of the device stack model at the start and end of the 500 ps MD simulation discussed above. We saw that the anode and cathode carried net positive and negative charges, respectively, after the voltage was applied across the initial relaxed structure (Figure ?? (a)), as expected. Consequently, the electrodes would have repelled (attracted) the ions in the functional layers that had charges of the same (opposite) polarities. The resultant movement of the ions, as discussed in the previous section, led to a redistribution of the net charges within the functional layer after the 500 ps of MD simulation under the applied voltage, as shown in Figure 6 (b), minimizing the total electrostatic energy. Notably, a thin top region of the dielectric at the interface with the anode, which is above the 50 Åz position, carries a significantly high net negative charge. This can be attributed to this thin region in the dielectric mainly consisting of the negatively charged O ions or anions and being nearly devoid of any cations (Figure 4 (a and b)) - as a result of the Ta ions being pushed away (downwards) from the anode interface (Figure 5 (a)). On the other hand, the increase in the net positive charge close to the cathode, which is below the 0 Åz position, in the dielectric layers (Figure 6 (b)) is smaller in magnitude as compared to the increase in the net negative charge near the anode. This could be attributed to the fact that this increase is due to the higher accumulation of Hf ions in the dielectric layer near the cathode while, in this case, the concentration of anions remains fairly consistent in the same region (Figure 4 (a and d)).

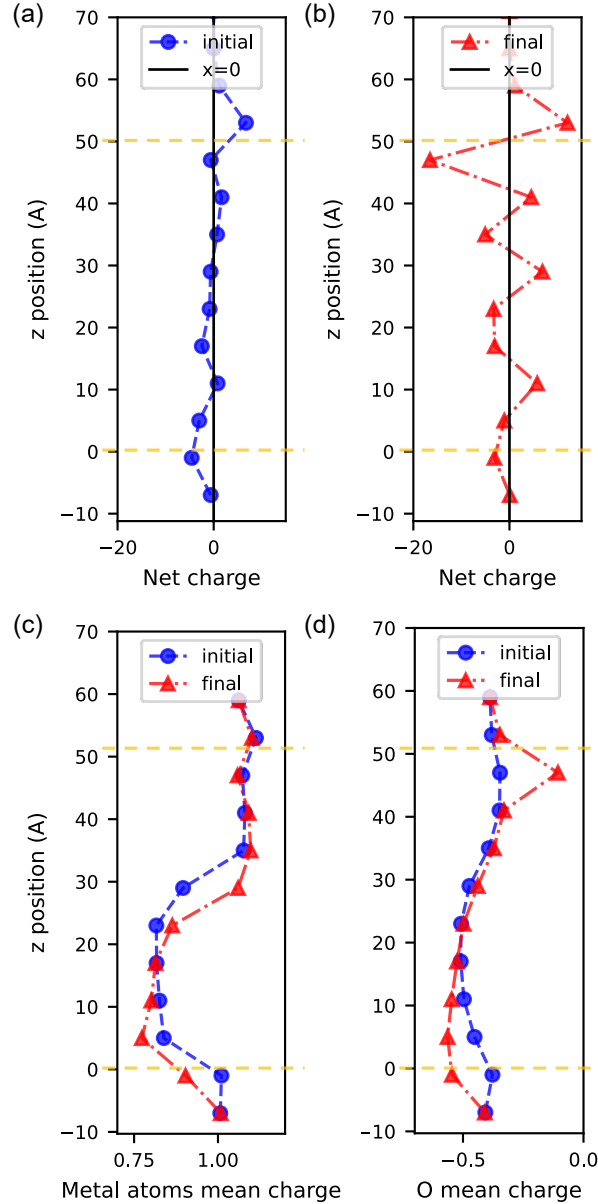


Figure 6: Distribution of ionic charges across the device stack model at the start and end of 500 ps MD simulation at 300 K and under 1.2 V difference across the electrodes. The variation of total charge on all atoms across the thickness of the (a) initial (after the voltage is applied to the relaxed structure but before any subsequent MD simulation) and (b) final (end of the 500 ps simulation) device stack model. The initial point corresponds to after the charges on all the atoms were equilibrated for the first time after application of the voltage in the initial structure. (c) and (d) plot the variation of the mean charges on the metal and oxygen ions, respectively, along the z-direction in both the initial and final device structures. The upper and lower dotted yellow lines in each subplot mark the location of the interfaces of the functional layers with the anode and the cathode, respectively, in the device model.

The reasons as to why the cations underwent significant voltage-driven displacement within the dielectric, including being repelled away from the anode, while, in contrast, the O anions did not get affected as strongly, could be understood by taking a closer look at the mean per atom charges on each ionic species. From Figures 6(c and d), we note that the magnitude of atomic charges on the metal ions remains significantly higher than that on the O ions, with the charges on the Ta ions being more than double those on the O ions (as can be seen for the plots corresponding to both the initial and final structures in Figures 6(c and d)). Consequently, the electrostatic forces on the metal cations due to the charges on the electrodes are much stronger as compared to those on the O anions, resulting in the observed characteristically different voltage-driven response of each ionic species (Figure 4 and Figure 5(a)). Interestingly, one can note from Figure 6(d) that in the final structure, the mean charges on the oxygen atoms in the thin dielectric region close to the anode (top electrode) got reduced to almost 0. This aligns well with the expectation based on our previous observations that the thin region on top of the dielectric layers near the anode is almost devoid of any metal ions (Figure 4(b)), as the ionic charges are primarily determined by their chemical environment.³⁴

In fact, such a redistribution of ions with opposing charge polarities at both the electrode interfaces of the functional layers (Figure 6(b)) in response to the applied electric potentials should effectively shield the ions within the dielectric matrix from majority of the external electric field. This could explain the need to apply a particularly high voltage of 5.85 V, which can overcome this shielding effect, in order to electroform these TaO_x/HfO₂-based ReRAM devices as observed in the experiments.¹⁴ This shielding of the bulk ions from the external electric field also subdues the ability of the applied voltage on the electrodes to cause continuous generation and migration of defects that could lead to filament growth, which is one of the key processes in the VCM model.

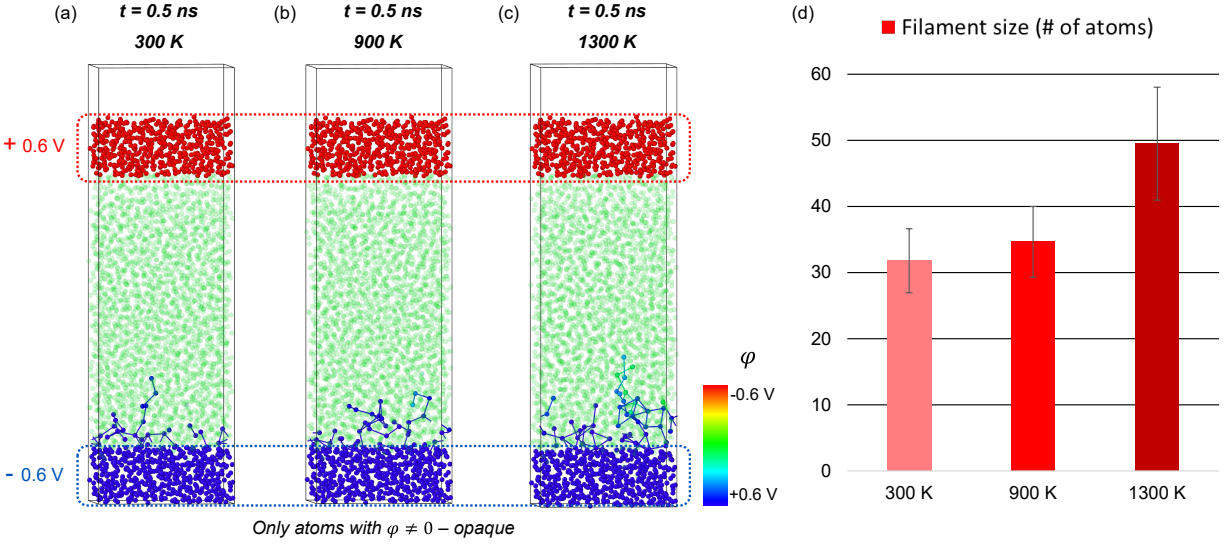


Figure 7: Effect of temperature on the growth of filament after 500 ps simulation under 1.2 V difference across the electrodes. Atomic snapshots of the final device structures post simulations at (a) 300 K, (b) 900 K, and (c) 1300 K, respectively. All the atoms with a 0 V electrochemical potential have been made semi-transparent. Consequently, only the electrode atoms and conductive cations that form the filament at the cathode interface are colored opaque. This is because the electrochemical potential applied to the cathode propagates through the conductive filament atoms, as indicated by the color coding. (d) The number of atoms in the filament for each temperature, averaged over the final 100 ps of simulation time with the error bars showing the corresponding standard deviations.

Effect of Joule Heating on the Atomistic Forming Mechanisms

To investigate the mechanism of filament formation and growth under Joule Heating in these devices, we repeated the simulation of our device model at two different temperatures of 900 K and 1300 K under the same voltage condition of 1.2 V across the electrodes. These higher temperatures were selected based on two reported values of maximum internal temperatures at the onset of forming in two different TaO₂-based devices, respectively, that also had inert electrodes.¹⁰ Although the overall composition profiles, including the oxygen-rich region near the anode, for these two higher temperatures at the end of the simulations run for 500 ps were similar to that for the earlier simulation at room temperature (Figure ??), there were notable differences between the extents of filament growth at each temperature. Figure 7 shows the final atomistic snapshots, with the atoms forming the filaments color-coded to

distinguish them from the rest of the dielectric matrix, and filament sizes, calculated as the average number of metallic ions forming the filament, for all the three simulations (at 300 K, 900 K and 1300 K) performed under an applied voltage of 1.2 V. These results indicated that the size of the nucleated filament increases significantly with temperature, especially at the high temperatures of 1300 K in the functional layers (7 (d)).

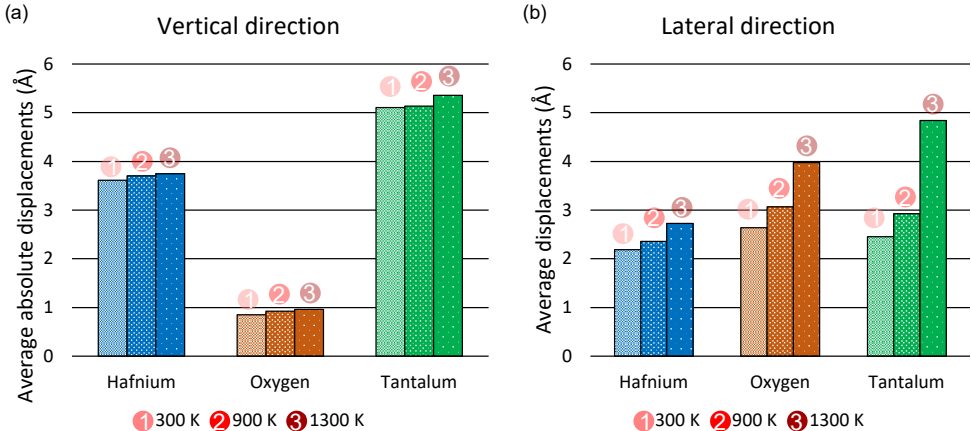


Figure 8: The change in average displacements of different ions for varying temperatures over 500 ps of MD simulation under 1.2 V difference across the electrodes. The average absolute displacements along the (a) vertical and (b) lateral directions in the device stack models.

In order to have a deeper understanding of the atomic processes underlying the filament growth at varying temperatures, we looked at the average net displacement of each atom type for the three 500 ps simulations, plotted in Figure 8. Interestingly, the absolute displacement of each ionic species in the vertical direction, which is parallel to the external electric field, increased only by a small amount on increasing the temperature (Figure 8 (a)). These results indicate that the increase in the size of the filament at higher temperatures cannot be primarily attributed to thermally activated increase in the vertical defect migration along the direction of the external electric field. This is in contrast to what is understood in the VCM model.³

On the other hand, the lateral motion of the ions, which is predominantly thermally activated, increased significantly with temperature, with a notably high increase at 1300 K for the O and Ta ions (Figure 8 (b)). In fact, at 1300 K, the lateral motion of the Ta ions be-

came even higher than that of the O ions, while the latter dominated at the temperatures of 300 K and 900 K (Figure 8 (b)). It is reasonable to assume that the high thermally activated motion of the ions (Figure 8 (b)) corresponds to an increased rate of bond breakage and O vacancy defect generation in the functional layers of the device, getting notably more pronounced at elevated temperatures (1300 K in our simulations). The generated O vacancies near the top end of the pre-seeded filament get stabilized by the negative charges from the filament,⁵⁰ which acts as a virtual cathode during forming.³ These nearby newly generated O vacancies should then agglomerate and combine with the existing filament, driven by the localized electric fields,⁹ growing it in size (Figure 7 (a-c)). These results further corroborate, and help elucidate the nature of, the crucial role of the thermal effects in accelerating filament formation through a mechanism of thermally-driven increased defect generation in the vicinity of the growing electrodes.

In fact, this mechanism that gets significantly more pronounced when the temperature reaches 1300 K in our simulations (Figures 7 (b) and 8 (b)) can also explain the compositional runaway effect observed in other TaO_x and HfO₂-based ReRAMs and the associated abrupt acceleration of filament growth during the electroforming process when the local temperature inside the device gets high enough.^{8,10,24,25}

Based on this understanding that the internal local temperature is the key factor underlying forming of the TaO_x/HfO₂ ReRAM, we can expect that increasing the device's overall temperature should reduce the required forming voltage. This is because an already higher device temperature would reduce the current density requirement for reaching the necessary internal temperatures in the functional layer by Joule heating for forming. We have also been experimentally verified this hypothesis by heating similar bilayer metal oxide-based ReRAM devices during electroforming, and observed a strong linear correlation between the temperature of the device and the required peak electroforming voltage, as reported in the Supplementary Information Figure S1.

Device Response under Low Voltage Conditions

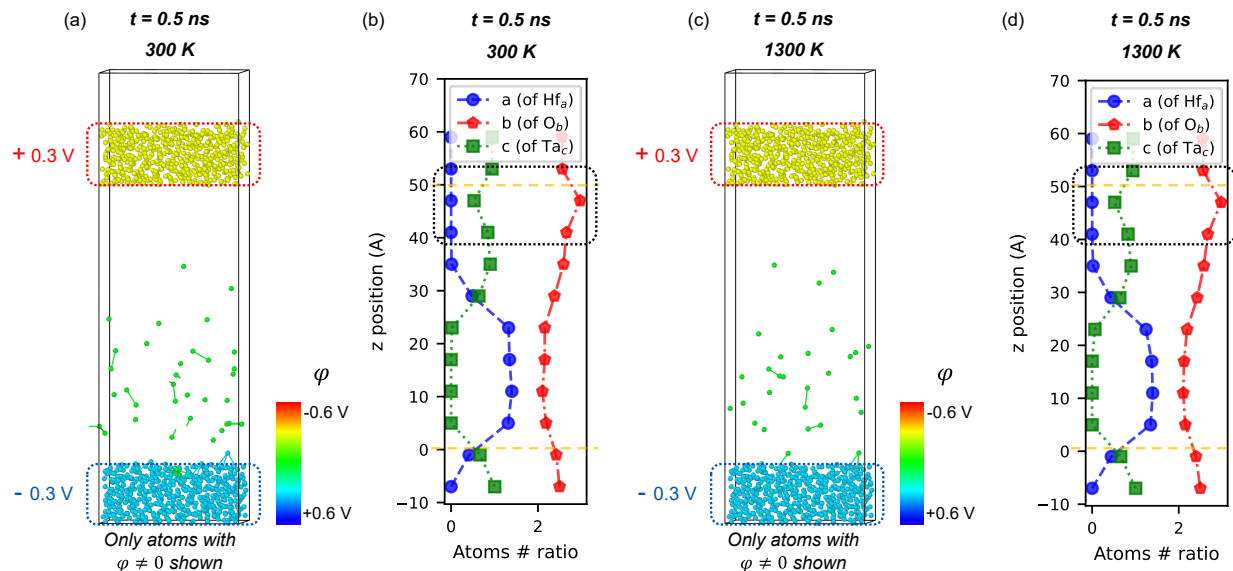


Figure 9: Effect of temperature on the vacancy distribution and composition change in the device stack after 500 ps simulation with a 0.6 V difference applied across the electrodes. (a) and (b) show the atomic snapshots of the device models simulated at 300 K and 1300 K, respectively. Only the electrode atoms and the conductive metal ions are visualized for clarity. (b) and (d) plot the profiles of the varying proportion of different ions within the device stack at the end of the corresponding simulations done at 300 K and 1300 K, respectively. The a, b, and c values, corresponding to the proportion of Hf, O, and Ta atoms, respectively, in the structure at any position along the z-axis, are normalized so that $a + b + c$ equals 3.5. The upper and lower dotted yellow lines in each subplot mark the location of the interfaces of the functional layers with the anode and the cathode, respectively, in the device model.

We next simulated our device model for 500 ps under 0.6 V applied across the electrodes, first at 300 K and then at the elevated temperature of 1300 K in order to differentiate its response and the thermal affects under a lower voltage from that at the onset of forming as discussed above. The state of vacancy distribution in the final structures and the final composition profiles are shown in Figure 9. We note that at 300 K, the vacancies did not agglomerate to initialize the filament formation in the device (Figure 9(a)), while an oxygen-rich region still developed near the anode (Figure 9(a-b)). We observe similar results at 1300 K as well under the 0.6 V applied bias (Figure 9 (c-d)), i.e., the vacancies still could not cluster together to start filament formation even at the elevated temperature (Figure 9 (c)).

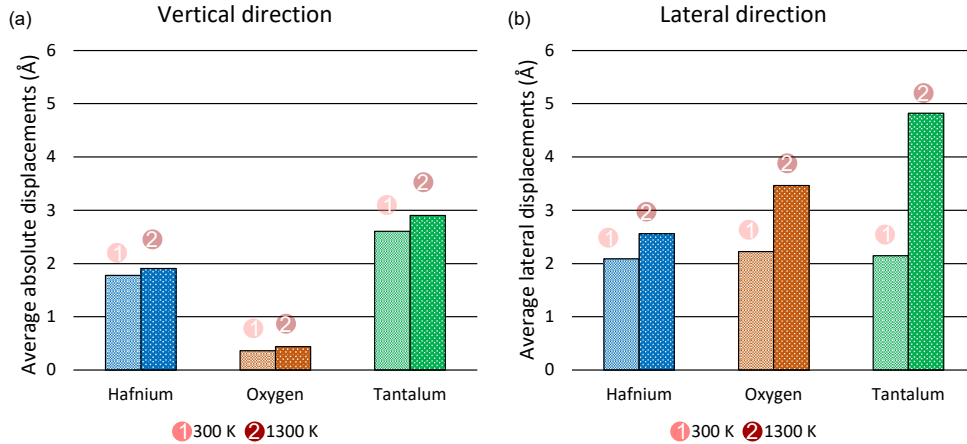


Figure 10: The change in average displacements of different ions for different temperatures over 500 ps of MD simulation under 0.6 V difference applied across the electrodes. The average absolute displacements along the (a) vertical and (b) lateral directions in the device stack models.

We further examined the ionic motion under a 0.6 V bias, as shown in 10. We observed that increasing the temperature to 1300 K affects the ionic mobilities in the same way as when a higher 1.2 V bias is applied (Figure 8). Specifically, the increased temperature significantly enhances the lateral motion of the ions, primarily for Ta, followed by O ions. However, despite this increased mobility on increasing the temperature, which was attributed as the cause for accelerating the filament growth under the 1.2 V applied voltage, no filament nucleation occurs under the low bias condition. This suggests that the applied voltage plays a critical role in the electroforming process beyond just causing the drift of vacancy defects towards the cathode. The external voltage helps overcome the repulsion between vacancies, allowing them to cluster together and form a conductive network.

This highlights an important finding that the formation of filament in $\text{TaO}_x/\text{HfO}_2$ -based ReRAMs can only occur if the applied voltage exceeds a certain threshold. Therefore, while thermal effects can accelerate filament growth, they only have a significant impact when the applied voltage surpasses this threshold in a given bilayer ReRAM device.

In this study, we revealed the detailed atomistic forming mechanisms in the bilayer $\text{TaO}_x/\text{HfO}_2$ -based ReRAM and clarified their physical underpinnings. These insights are

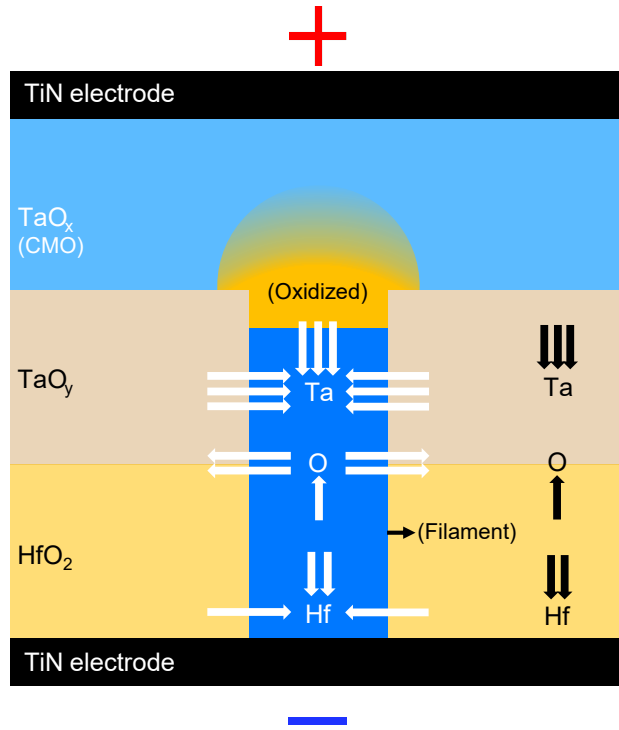


Figure 11: Schematic illustrating the possible atomic movements underlying forming in $\text{TaO}_x/\text{HfO}_2$ ReRAM devices. The number of arrows qualitatively represents the relative magnitudes of displacement of each ion in different directions and across different regions within the device.

illustrated in Figure 11, which includes a schematic of a possible final structure of the formed ReRAM device. The atomic movements behind the forming are qualitatively represented by arrows, with their number indicating the relative magnitudes of displacement for each ion in different directions and regions within the device. The temperature and voltage-driven motion of the different ionic species as observed in this study for both the functional layers indicates that the filament formation occurs across both the functional dielectric layers in the $\text{TaO}_x/\text{HfO}_2$ -based ReRAM devices, along with the creation of an oxygen-rich region at the interface between the conductive TaO_x and dielectric TaO_y layers. The extension of the oxidized region into the TaO_x layer on top of the filament, as proposed in prior experimental studies,¹⁴ could occur at the high temperatures reached during forming as a result of Fick's diffusion¹⁰ of oxygen ions accumulated at the interface.

Conclusion

We performed MD simulations on a $\text{TaO}_x/\text{HfO}_2$ resistive switching device by locally applying voltage on inert electrodes employing an extended CTIP formalism for multi-metal oxide systems to use together with the EChemDID method. We found that the application of high voltage on the pristine model leads to the filament nucleating at the negative bottom electrode, or cathode, interface. This was accompanied by the development of an oxygen-rich zone at the anodic (the conductive top layer of the device acting as the extension of the top electrode) interface of the dielectric Ta_2O_5 interlayer due to the repulsion of the Ta atoms away from the anode. Furthermore, the Ta and Hf ions underwent notably greater vertical displacements than the oxygen ions in the direction of the external electric field, which is attributed to their increased per-atom charges.

On increasing the temperature up to 1300 K, we observed a significant increase in the size of the nucleated filament, in terms of the number of metallic ions that are part of the filament at the end of the simulation. This was accompanied by significantly enhanced lateral displacements of the ions, particularly of O and Ta ions, and only a minor increase in the vertical voltage-driven ionic migration. Thus, the role of temperature in accelerating filament growth was attributed to a thermally activated increase in the generation of O vacancy defects. These defects get stabilized in the vicinity of the growing filament, which acts as the virtual cathode, and aggregate with it to cause rapid filament growth.

We also found the existence of a threshold voltage beyond which the oxygen vacancies in the functional layer can overcome their mutual repulsion and cluster together near the cathode enabling filament nucleation. This coupled temperature and electric field-driven mechanism can explain the previous reports of these devices exhibiting behavior characteristic of both the VCM and TCM models. We also experimentally observed that increasing the chip temperature reduced the forming voltage of a metal oxide-based bilayer ReRAM device, which aligned well with the role of the thermally-driven filament forming mechanisms in these devices deduced from our simulations.

The mechanistic insights from this study provide a clear atomic-level understanding of the various processes underlying the forming behavior of the TaO_x/HfO₂ ReRAM devices. Notably, we found that the local electric field and Joule heating in the device combine to accelerate filament growth during forming through an interfacial mechanism of defect generation, stabilization, and agglomeration. This alleviates the requirement of continuous anodic electro-reduction of the dielectric and the subsequent electro-migration of the oxygen vacancies for electroforming, which is part of the VCM model. These insights are expected to not only guide future optimization and deliberate improvements in the device design, but also the development of more physics-accurate analytical and compact models for emulating the behavior of these devices for circuit-level simulations.

In addition, the extended CTIP + EChemDID formulation has been implemented in this study and made available as an additional package for the open-source simulation tool, LAMMPS. We note that the actual electroforming process could occur over a timescale of several μs , which is beyond the accessible range of all-atom variable charge MD simulations. Hence, the conclusions derived in this study are focused on the initial mechanisms governing the early stage filament formation in the bilayer ReRAM device, and more work is needed to deduce conclusive insights on the structure and behavior of the device at the end of the forming process.

Computational Methods

Interatomic Potential and Charge Dynamics

Atomic interactions were modeled using a hybrid reactive potential of the form proposed by Zhou et al. combining the charge transfer ionic potential (CTIP) for electrostatic energy and a modified embedded atom method (EAM) for non-electrostatic contributions.^{35,40} The total energy, E , can be partitioned as:

$$E = E_{es} + E_{ne}. \quad (1)$$

E_{es} is the electrostatic contribution given as ⁴⁰

$$\begin{aligned} E_{es} = & E_0 + \sum_{i=1}^N q_i \chi_i + \frac{1}{2} \sum_{i=1}^N \sum_{j=1}^N q_i q_j V_{ij} + \sum_{i=1}^N \omega \left(1 - \frac{q_i - q_{min,i}}{|q_i - q_{min,i}|} \right) (q_i - q_{min,i})^2 \\ & + \sum_{i=1}^N \omega \left(1 - \frac{q_{max,i} - q_i}{|q_{max,i} - q_i|} \right) (q_{max,i} - q_i)^2, \end{aligned} \quad (2)$$

wherein N represents the number of atoms in the system, $q_{min,i}$ and $q_{max,i}$ represents the bounds for the charges on an atom i , which is imposed by an energy penalty when the charge is beyond these bounds. The strictness of the bounds is determined by the coefficient ω .⁴⁰ χ_i and V_{ij} represent the electronegativity and the electrostatic potential contribution arising from the interaction between partial charges on atoms i and j , respectively. The values of these parameters optimized for several multi-metal oxide systems have been obtained from the literature.⁴⁰

The non-electrostatic contribution, E_{ne} , described by Zhou and Wadley³⁵ is given as:

$$E_{ne} = \frac{1}{2} \sum_{i=1}^N \sum_{j=i_1}^{i_M} \varphi_{ij}(r_{ij}) + \sum_{i=1}^N F_i(\rho_i), \quad (3)$$

The value tables for ρ_i , F_i , and φ_{ij} for different interatomic separation distances have been calculated using suitable functional forms and optimized parameters for systems comprising of oxides of multiple transition metals in literature.^{40,42,43} The atomic charge equilibration was achieved through the electronegativity equalization method (EEM).⁵¹

External Electrochemical Potential Propagation Method

To simulate bias-induced redox reactions and filament formation in the system, the electrochemical dynamics with implicit degrees of freedom (EChemDID) method³⁷ was imple-

mented in LAMMPS. In this method, an external voltage, Φ_0 , was applied by adding a suitable value of the local potential (Φ) to the electronegativity of electrode atoms as $\chi_0 - \Phi_0/2$ for the anode or the positive electrode (i.e., $\Phi = -\Phi_0/2$), and $\chi_0 + \Phi_0/2$ for the cathode or the negative electrode (i.e., $\Phi = \Phi_0/2$).³⁷ The metallic atoms were identified as the Ta and Hf atoms with oxygen coordination ≤ 5 and the local potentials of all the metallic atoms connected with either of the electrodes were updated each 50 ps during the MD simulation via a computationally efficient nonphysical diffusion equation³⁷ as follows:

$$\dot{\Phi} = k \sum_{k \neq i} \frac{\Phi_i(t) - \Phi_j(t)}{|R_{ij}|^2} w(R_{ij}), \quad (4)$$

In Equation 4, $w(R_{ij})$ is a weight function calculated as

$$w(R_{ij}) = \begin{cases} N \left[1 - \left(\frac{R_{ij}}{R_C} \right)^2 \right]^2 & \text{if } R_{ij} < R_C \\ 0 & \text{otherwise} \end{cases} \quad (5)$$

wherein N is a normalization constant, taken as 0.5, and R_C is the cutoff radius, taken as 3.9 Å, for two metallic atoms to be part of the same cluster. This diffusive step is run for 10 iterations before calculation of the atomic charges based on the updated electronegativities of the atoms and resuming the MD simulations.⁹ This helps to capture the dynamically varying filament in the structure and the consequent effects on the ionic dynamics, including the filament evolution itself, through the localized, and evolving, electric field within the material. A timestep of 0.2 fs was adopted for the MD simulations

Supporting Information

Figure S1 and Figure S2 are provided.

Acknowledgement

The authors thank the European Union’s Horizon Europe research and innovation program under PHASTRAC project grant agreement No. 101092096 for funding this study.

References

1. Chen, Y. Y.; Govoreanu, B.; Goux, L.; Degraeve, R.; Fantini, A.; Kar, G. S.; Wouters, D. J.; Groeseneken, G.; Kittl, J. A.; Jurczak, M.; others Balancing SET/RESET Pulse for $> 10^{10}$ Endurance in HfO₂/Hf_{1T1R} Bipolar RRAM. *IEEE Transactions on Electron devices* **2012**, *59*, 3243–3249.
2. Lee, M.-J.; Lee, C. B.; Lee, D.; Lee, S. R.; Chang, M.; Hur, J. H.; Kim, Y.-B.; Kim, C.-J.; Seo, D. H.; Seo, S.; others A fast, high-endurance and scalable non-volatile memory device made from asymmetric Ta₂O₅-x/TaO₂-x bilayer structures. *Nature materials* **2011**, *10*, 625–630.
3. Dittmann, R.; Menzel, S.; Waser, R. Nanoionic memristive phenomena in metal oxides: the valence change mechanism. *Advances in Physics* **2021**, *70*, 155–349.
4. Ma, Y.; Goodwill, J. M.; Li, D.; Cullen, D. A.; Poplawsky, J. D.; More, K. L.; Bain, J. A.; Skowronski, M. Stable Metallic Enrichment in Conductive Filaments in TaO_x-Based Resistive Switches Arising from Competing Diffusive Fluxes. *Advanced Electronic Materials* **2019**, *5*, 1800954.
5. Cartoixa, X.; Rurali, R.; Sune, J. Transport properties of oxygen vacancy filaments in metal/crystalline or amorphous HfO₂/metal structures. *Physical Review B—Condensed Matter and Materials Physics* **2012**, *86*, 165445.
6. Rosário, C. M.; Thöner, B.; Schönhals, A.; Menzel, S.; Wuttig, M.; Waser, R.; Sobolev, N. A.; Wouters, D. J. Correlation between the transport mechanisms in conduc-

- tive filaments inside Ta₂O₅-based resistive switching devices and in substoichiometric TaO_x thin films. *Applied physics letters* **2018**, *112*.
7. Rosário, C. M.; Thöner, B.; Schönhals, A.; Menzel, S.; Meledin, A.; Barradas, N. P.; Alves, E.; Mayer, J.; Wuttig, M.; Waser, R.; others Metallic filamentary conduction in valence change-based resistive switching devices: the case of TaO_x thin film with $x < 1$. *Nanoscale* **2019**, *11*, 16978–16990.
 8. Ma, Y.; Li, D.; Herzing, A. A.; Cullen, D. A.; Sneed, B. T.; More, K. L.; Nuhfer, N.; Bain, J. A.; Skowronski, M. Formation of the conducting filament in TaO_x-resistive switching devices by thermal-gradient-induced cation accumulation. *ACS applied materials & interfaces* **2018**, *10*, 23187–23197.
 9. Urquiza, M. L.; Islam, M. M.; Van Duin, A. C.; Cartoixà, X.; Strachan, A. Atomistic insights on the full operation cycle of a HfO₂-based resistive random access memory cell from molecular dynamics. *ACS nano* **2021**, *15*, 12945–12954.
 10. Ma, Y.; Cullen, D. A.; Goodwill, J. M.; Xu, Q.; More, K. L.; Skowronski, M. Exchange of Ions across the TiN/TaO_x Interface during Electroformation of TaO_x-Based Resistive Switching Devices. *ACS applied materials & interfaces* **2020**, *12*, 27378–27385.
 11. Yao, P.; Wu, H.; Gao, B.; Eryilmaz, S. B.; Huang, X.; Zhang, W.; Zhang, Q.; Deng, N.; Shi, L.; Wong, H.-S. P.; others Face classification using electronic synapses. *Nature communications* **2017**, *8*, 15199.
 12. Woo, J.; Moon, K.; Song, J.; Lee, S.; Kwak, M.; Park, J.; Hwang, H. Improved synaptic behavior under identical pulses using AlO_x/HfO₂ bilayer RRAM array for neuromorphic systems. *IEEE Electron Device Letters* **2016**, *37*, 994–997.
 13. Cüppers, F.; Menzel, S.; Bengel, C.; Hardtdegen, A.; Von Witzleben, M.; Böttger, U.; Waser, R.; Hoffmann-Eifert, S. Exploiting the switching dynamics of HfO₂-based ReRAM devices for reliable analog memristive behavior. *APL materials* **2019**, *7*.

14. Stecconi, T.; Guido, R.; Berchialla, L.; La Porta, A.; Weiss, J.; Popoff, Y.; Halter, M.; Sousa, M.; Horst, F.; Dávila, D.; others Filamentary TaOx/HfO2 ReRAM Devices for Neural Networks Training with Analog In-Memory Computing. *Advanced electronic materials* **2022**, *8*, 2200448.
15. Stecconi, T.; Bragaglia, V.; Rasch, M. J.; Carta, F.; Horst, F.; Falcone, D. F.; Ten Kate, S. C.; Gong, N.; Ando, T.; Olziersky, A.; others Analog resistive switching devices for training deep neural networks with the novel tiki-taka algorithm. *Nano Letters* **2024**, *24*, 866–872.
16. Wan, W.; Kubendran, R.; Schaefer, C.; Eryilmaz, S. B.; Zhang, W.; Wu, D.; Deiss, S.; Raina, P.; Qian, H.; Gao, B.; others A compute-in-memory chip based on resistive random-access memory. *Nature* **2022**, *608*, 504–512.
17. Gong, N.; Rasch, M. J.; Seo, S.-C.; Gasasira, A.; Solomon, P.; Bragaglia, V.; Consiglio, S.; Higuchi, H.; Park, C.; Brew, K.; others Deep learning acceleration in 14nm CMOS compatible ReRAM array: device, material and algorithm co-optimization. 2022 International Electron Devices Meeting (IEDM). 2022; pp 33–7.
18. Falcone, D. F.; Clerico, V.; Choi, W.; Stecconi, T.; Horst, F.; Begon-Lours, L.; Galetta, M.; La Porta, A.; Garg, N.; Alibart, F.; others All-in-One Analog AI Accelerator: On-Chip Training and Inference with Conductive-Metal-Oxide/HfOx ReRAM Devices. *arXiv preprint arXiv:2502.04524* **2025**,
19. Delacour, C.; Carapezzi, S.; Abernot, M.; Boschetto, G.; Azemard, N.; Salles, J.; Gil, T.; Todri-Sanial, A. Oscillatory neural networks for edge ai computing. 2021 IEEE computer society annual symposium on VLSI (ISVLSI). 2021; pp 326–331.
20. Todri-Sanial, A.; Delacour, C.; Abernot, M.; Sabo, F. Computing with oscillators from theoretical underpinnings to applications and demonstrators. *Npj unconventional computing* **2024**, *1*, 1–16.

21. Galetta, M.; Falcone, D. F.; Menzel, S.; La Porta, A.; Stecconi, T.; Choi, W.; Offrein, B. J.; Bragaglia, V. Compact Model of Conductive-Metal-Oxide/HfO_x Analog Filamentary ReRAM Devices. 2024 IEEE European Solid-State Electronics Research Conference (ESSERC). 2024; pp 749–752.
22. Falcone, D. F.; Menzel, S.; Stecconi, T.; Galetta, M.; La Porta, A.; Offrein, B. J.; Bragaglia, V. Analytical modelling of the transport in analog filamentary conductive-metal-oxide/HfO_x ReRAM devices. *Nanoscale Horizons* **2024**, *9*, 775–784.
23. Falcone, D. F.; Menzel, S.; Stecconi, T.; La Porta, A.; Carraria-Martinotti, L.; Offrein, B. J.; Bragaglia, V. Physical modeling and design rules of analog Conductive Metal Oxide-HfO₂ ReRAM. 2023 IEEE International Memory Workshop (IMW). 2023; pp 1–4.
24. Kumar, S.; Wang, Z.; Huang, X.; Kumari, N.; Davila, N.; Strachan, J. P.; Vine, D.; Kilcoyne, A. D.; Nishi, Y.; Williams, R. S. Conduction channel formation and dissolution due to oxygen thermophoresis/diffusion in hafnium oxide memristors. *ACS nano* **2016**, *10*, 11205–11210.
25. Kumar, S.; Graves, C. E.; Strachan, J. P.; Grafals, E. M.; Kilcoyne, A. L. D.; Tyliczszak, T.; Weker, J. N.; Nishi, Y.; Williams, R. S. Direct Observation of Localized Radial Oxygen Migration in Functioning Tantalum Oxide Memristors. *Advanced Materials* **2016**, *28*, 2771–2771.
26. Waser, R.; Dittmann, R.; Staikov, G.; Szot, K. Redox-Based Resistive Switching Memories-Nanoionic Mechanisms, Prospects, and Challenges. *Advanced Materials (Deerfield Beach, Fla.)* **2009**, *21*, 2632–2663.
27. Padovani, A.; Larcher, L.; Padovani, P.; Cagli, C.; De Salvo, B. Understanding the role of the Ti metal electrode on the forming of HfO₂-based RRAMs. 2012 4th IEEE International Memory Workshop. 2012; pp 1–4.

28. Jeong, D. S.; Schroeder, H.; Breuer, U.; Waser, R. Characteristic electroforming behavior in Pt/TiO₂/Pt resistive switching cells depending on atmosphere. *Journal of applied physics* **2008**, *104*.
29. Goodwill, J. M.; Ramer, G.; Li, D.; Hoskins, B. D.; Pavlidis, G.; McClelland, J. J.; Centrone, A.; Bain, J. A.; Skowronski, M. Spontaneous current constriction in threshold switching devices. *Nature communications* **2019**, *10*, 1628.
30. Russo, U.; Ielmini, D.; Cagli, C.; Lacaita, A. L. Self-accelerated thermal dissolution model for reset programming in unipolar resistive-switching memory (RRAM) devices. *IEEE Transactions on Electron Devices* **2009**, *56*, 193–200.
31. Ielmini, D.; Bruchhaus, R.; Waser, R. Thermochemical resistive switching: materials, mechanisms, and scaling projections. *Phase Transitions* **2011**, *84*, 570–602.
32. Son, J.; Shin, Y.-H. Direct observation of conducting filaments on resistive switching of NiO thin films. *Applied Physics Letters* **2008**, *92*.
33. Goodwill, J. M.; Sharma, A. A.; Li, D.; Bain, J. A.; Skowronski, M. Electro-thermal model of threshold switching in TaO_x-based devices. *ACS applied materials & interfaces* **2017**, *9*, 11704–11710.
34. Xiao, B.; Yu, X.; Watanabe, S. A comparative study on the diffusion behaviors of metal and oxygen ions in metal-oxide-based resistance switches via ab initio molecular dynamics simulations. *ACS Applied Electronic Materials* **2019**, *1*, 585–594.
35. Zhou, X.; Wadley, H.; Filhol, J.-S.; Neurock, M. Modified charge transfer–embedded atom method potential for metal/metal oxide systems. *Physical Review B* **2004**, *69*, 035402.
36. Zhou, X. W.; Wadley, H. N. A charge transfer ionic–embedded atom method potential for the O–Al–Ni–Co–Fe system. *Journal of Physics: Condensed Matter* **2005**, *17*, 3619.

37. Onofrio, N.; Strachan, A. Voltage equilibration for reactive atomistic simulations of electrochemical processes. *The Journal of chemical physics* **2015**, *143*.
38. Rappe, A. K.; Goddard III, W. A. Charge equilibration for molecular dynamics simulations. *The Journal of Physical Chemistry* **1991**, *95*, 3358–3363.
39. Lee, E.; Lee, K.-R.; Baskes, M.; Lee, B.-J. A modified embedded-atom method interatomic potential for ionic systems: 2 nnmeam+ qeq. *Physical Review B* **2016**, *93*, 144110.
40. Wu, Y.; Yu, W.; Shen, S. Developing a variable charge potential for Hf/Nb/Ta/Ti/Zr/O system via machine learning global optimization. *Materials & Design* **2023**, *230*, 111999.
41. Streit, F.; Mintmire, J. Electrostatic potentials for metal-oxide surfaces and interfaces. *Physical Review B* **1994**, *50*, 11996.
42. Sasikumar, K.; Narayanan, B.; Cherukara, M.; Kinaci, A.; Sen, F. G.; Gray, S. K.; Chan, M. K.; Sankaranarayanan, S. K. Evolutionary optimization of a charge transfer ionic potential model for Ta/Ta-Oxide heterointerfaces. *Chemistry of Materials* **2017**, *29*, 3603–3614.
43. Sasikumar, K.; Chan, H.; Narayanan, B.; Sankaranarayanan, S. K. Machine learning applied to a variable charge atomistic model for Cu/Hf binary alloy oxide heterostructures. *Chemistry of Materials* **2019**, *31*, 3089–3102.
44. Onofrio, N.; Guzman, D.; Strachan, A. Atomic origin of ultrafast resistance switching in nanoscale electrometallization cells. *Nature materials* **2015**, *14*, 440–446.
45. Plimpton, S. Fast parallel algorithms for short-range molecular dynamics. *Journal of computational physics* **1995**, *117*, 1–19.
46. Stecconi, T.; Popoff, Y.; Guido, R.; Falcone, D.; Halter, M.; Sousa, M.; Horst, F.; La Porta, A.; Offrein, B. J.; Bragaglia, V. Role of Conductive-Metal-Oxide to HfO_x, In-

- terfacial Layer on the Switching Properties of Bilayer TaO_x/HfO_x ReRAM. ESSDERC 2022-IEEE 52nd European Solid-State Device Research Conference (ESSDERC). 2022; pp 297–300.
47. Schönhals, A.; Rosario, C. M.; Hoffmann-Eifert, S.; Waser, R.; Menzel, S.; Wouters, D. J. Role of the electrode material on the RESET limitation in oxide ReRAM devices. *Advanced electronic materials* **2018**, *4*, 1700243.
48. Nosé, S. A unified formulation of the constant temperature molecular dynamics methods. *The Journal of chemical physics* **1984**, *81*, 511–519.
49. Hoover, W. G. Canonical dynamics: Equilibrium phase-space distributions. *Physical review A* **1985**, *31*, 1695.
50. Zeumault, A.; Alam, S.; Wood, Z.; Weiss, R. J.; Aziz, A.; Rose, G. S. TCAD modeling of resistive-switching of HfO₂ memristors: Efficient device-circuit co-design for neuro-morphic systems. *Frontiers in Nanotechnology* **2021**, *3*, 734121.
51. Mortier, W. J.; Ghosh, S. K.; Shankar, S. Electronegativity-equalization method for the calculation of atomic charges in molecules. *Journal of the American Chemical Society* **1986**, *108*, 4315–4320.